doi:10.1038/nature14035

Crystal structure of the human OX_2 orexin receptor bound to the insomnia drug suvorexant

Jie Yin[1], Juan Carlos Mobarec[2], Peter Kolb[2] & Daniel M. Rosenbaum[1]

The orexin (also known as hypocretin) G protein-coupled receptors (GPCRs) respond to orexin neuropeptides in the central nervous system to regulate sleep and other behavioural functions in humans[1]. Defects in orexin signalling are responsible for the human diseases of narcolepsy and cataplexy; inhibition of orexin receptors is an effective therapy for insomnia[2]. The human OX_2 receptor (OX_2R) belongs to the β branch of the rhodopsin family of GPCRs[3], and can bind to diverse compounds including the native agonist peptides orexin-A and orexin-B and the potent therapeutic inhibitor suvorexant[4]. Here, using lipid-mediated crystallization and protein engineering with a novel fusion chimaera, we solved the structure of the human OX_2R bound to suvorexant at 2.5 Å resolution. The structure reveals how suvorexant adopts a π-stacked horseshoe-like conformation and binds to the receptor deep in the orthosteric pocket, stabilizing a network of extracellular salt bridges and blocking transmembrane helix motions necessary for activation. Computational docking suggests how other classes of synthetic antagonists may interact with the receptor at a similar position in an analogous π-stacked fashion. Elucidation of the molecular architecture of the human OX_2R expands our understanding of peptidergic GPCR ligand recognition and will aid further efforts to modulate orexin signalling for therapeutic ends.

The orexin system modulates diverse behaviours in mammals, including sleep, arousal and feeding[1]. Orexin neurons in the lateral hypothalamus uniquely produce the 33-amino-acid orexin-A and 28-amino-acid orexin-B neuropeptides. Orexin receptors OX_1R and OX_2R, distributed throughout the central nervous system, respond to these peptides to control neuronal activity. Signals generated from the hypothalamus, the limbic system and the periphery converge on the orexin neurons, which act as central integrators of environmental cues and extend processes to many different brain centres. The orexin receptors belong to the rhodopsin family of GPCRs and relay neuropeptide binding at synapses into intracellular activation of heterotrimeric $G_{q/11}$ and $G_{i/o}$ (ref. 5). The importance of the orexin system in phasic control of sleep–wake cycles was highlighted by discoveries that disruption/deletion of orexin or OX_2R causes narcolepsy in dogs[6], mice[7] and humans[8]. As a result, a number of potent dual orexin receptor antagonists (DORAs) have been developed and tested over the past decade[4], culminating in US Food and Drug Administration (FDA) approval of the first-in-class drug suvorexant (Belsomra) for insomnia. Suvorexant binds to human OX_1R and OX_2R (hOX_1R and hOX_2R) with sub-nanomolar affinity, potently inhibits orexin receptor signalling in cell-based assays, and promotes the transition to rapid eye movement (REM) and slow wave sleep in animals and humans[2,4,9].

To understand better the molecular basis of orexin receptor ligand recognition and signalling, we sought to obtain a high-resolution X-ray crystal structure of hOX_2R. Protein engineering (fusion proteins[10] and thermostable mutants[11]) and lipid-mediated crystallization methods[12] have recently enabled the determination of the structures of GPCRs for diverse ligands such as biogenic amines, nucleotides, peptide hormones and lipids. OX_1R and OX_2R belong to the β branch of the rhodopsin family of GPCRs, which contains receptors for neuropeptides such as the tachykinins, oxytocin/vasopressin and neurotensin[3]. Crystal structures of thermostabilized mutants of the rat neurotensin receptor (NTSR1), in partially active[13] and inactive[14] conformations, constitute the only crystallographic data currently available for this physiologically important group of GPCRs. Our attempts to express and crystallize a hOX_2R–T4L fusion protein, an approach we originally developed for the β_2 adrenergic receptor (β_2AR)[10], were unsuccessful.

We therefore explored the use of alternative fusion protein partners that would help hOX_2R pack into a well-defined three-dimensional lattice. For candidate fusion partners, we searched for domains of fewer than 200 amino acids from extreme thermophiles, which had been previously crystallized and characterized by X-ray diffraction at high resolution and have amino and carboxy termini that are close (within 10 Å) in three-dimensional space. Using a construct in which the 196-amino-acid catalytic domain of *Pyrococcus abysii* glycogen synthase (PGS)[15] replaced 39 residues of the third intracellular loop (ICL3), we were able to grow microcyrstals of hOX_2R in a cholesterol-doped monoolein cubic phase (Extended Data Fig. 2) and solve the suvorexant-bound structure at 2.5 Å resolution (Extended Data Table 1). As expected, the PGS domain promotes tight packing of hOX_2R into a crystal lattice in which membrane layers containing the embedded GPCR alternate with aqueous layers containing the fusion partner (Fig. 1a).

The overall seven-transmembrane (TM) fold of hOX_2R resembles other GPCR structures (Fig. 1a, b). Despite a low sequence similarity (23% identity), the backbone root mean square deviation (r.m.s.d.) relative to the inactive-state β_2AR[10] is only 2.2 Å. The backbone r.m.s.d. compared with NTSR1 (22% identity) is 1.3 Å for the inactive-state[14] and 2.3 Å for the partial active-state conformation[13]. At the extracellular surface, residues 190–212 in the second extracellular loop (ECL2) form a β-hairpin (Fig. 1c, d) analogous to that seen in other peptide-binding GPCRs such as NTSR1 (ref. 13), the μ-opioid receptor[16] and CXCR4 (ref. 17)—this β-hairpin structure contains amino acids important for orexin binding and activation[18].

Superposition of suvorexant-bound hOX_2R with the antagonist-bound M3 muscarinic acetylcholine receptor[19], another G_q-coupled GPCR, shows a high degree of overlap between TM backbones at the intracellular surface (Fig. 1b). One difference is that the conserved 'DRY motif' on TM3, part of an inhibitory interaction network in the rhodopsin family of GPCRs[20], is 'DRWY' in hOX_2R. Residues $D151^{3.49}$ and $R152^{3.50}$ (superscripts are Ballesteros–Weinstein numbering throughout) make an intra-motif salt bridge, while $R152^{3.50}$ and $W153^{3.51}$ contact the cytoplasmic ends of TM5 and TM6 ($Q245^{5.60}$, $I246^{5.61}$ and $L306^{6.37}$). Overall, numerous hydrophobic and polar contacts bind TM5 and TM6 to the other TM domains, restricting the outward movement of these α-helices necessary for GPCR activation. The suvorexant-bound hOX_2R structure thus represents an inactive-state conformation, consistent with the efficacy profile of suvorexant as a DORA ligand.

The suvorexant-binding pocket is open to the extracellular space through a constricted solvent-accessible channel (Fig. 2a) rimmed by amino acids from the extracellular ends of TM2, TM5–7 and the ECL2 β-hairpin. A complex network of electrostatic interactions covers the

---

[1]Department of Biophysics, The University of Texas Southwestern Medical Center, Dallas, Texas 75390, USA. [2]Department of Pharmaceutical Chemistry, Philipps-University Marburg, 35032 Marburg, Germany.

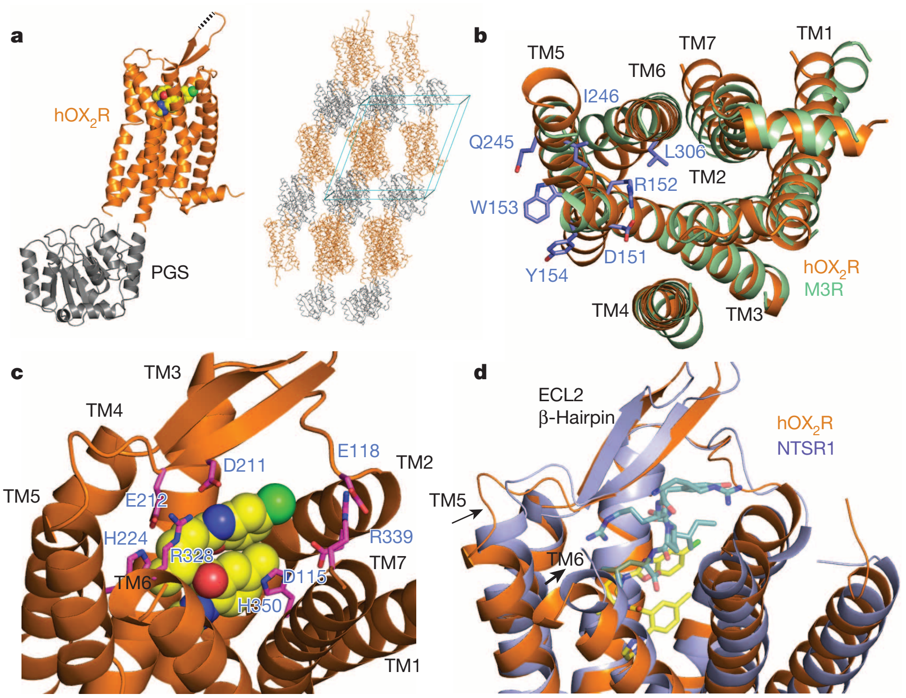

Figure 1 | Fusion protein engineering and structural features of hOX$_2$R. **a**, Left, global structure of the hOX$_2$R–PGS fusion protein. hOX$_2$R is represented as an orange cartoon, with the PGS domain (grey cartoon) fused at ICL3. Suvorexant is shown as spheres with yellow carbons. Dotted line represents the five amino acids that could not be modelled at the tip of the β-hairpin in ECL2. Right, packing of the hOX$_2$R–PGS fusion protein in the lipidic-cubic-phase-derived crystal lattice. **b**, Overlap between suvorexant-bound hOX$_2$R (orange cartoon) and antagonist-bound M3R[19] (green cartoon; Protein Data Bank (PDB) accession 4DAJ) at the intracellular surface. The DRWY sequence on TM3 and interacting residues on TM5 and 6 are shown as blue sticks. **c**, Salt-bridge network at the extracellular surface of hOX$_2$R. Residues participating in electrostatic interactions are shown as magenta sticks, with suvorexant represented as spheres with yellow carbons. ECL3 is removed for clarity. **d**, Superposition of hOX$_2$R (orange cartoon) and NTSR1 (blue cartoon) in a partial active-state conformation (PDB accession 4GRV)[13]. Suvorexant (yellow carbons) and the NTS$_{8-13}$ agonist (teal carbons) are shown as transparent sticks. ECL3 is removed for clarity.

extracellular surface of the receptor, including salt bridges on both sides of the ligand entry channel (D115$^{2.65}$–H350$^{7.39}$, E118$^{2.68}$–R339$^{7.28}$, D211$^{45.51}$–R328$^{6.59}$, E212$^{45.52}$–H224$^{5.39}$) that stabilize the extracellular TM conformation (Figs 1c and 2a). A similar extracellular salt bridge in β_2AR (ECL2 to TM3) was previously shown to be a ligand-dependent switch by NMR spectroscopy[21]. Mutation of residue D211$^{45.51}$ to Ala has one of the greatest characterized deleterious effects on orexin-A potency, but has little impact on binding of some DORAs such as almorexant[18]—this amino acid is over 6 Å more extracellular than the closest suvorexant atom in the crystal structure. The difference between orexin and DORA sensitivity to D211A$^{45.51}$ suggests that modulation or competition of the extracellular salt bridges may be involved in orexin binding and activation of the receptor. In further support of this hypothesis, the neurotensin agonist peptide NTS$_{8-13}$ present in the partially active NTSR1 structure[13] occupies a more extracellular position than suvorexant, adjacent to the β-hairpin, stabilizing a slight inward movement of TM5 and TM6 (Fig. 1d). Such inward movements of TM5 and TM6 relative to the rest of the TM bundle at the orthosteric binding pocket may be a general trigger for agonist-mediated GPCR activation, as they have also been observed for the β_2AR[22] and the M2 muscarinic acetylcholine receptor[23].

Suvorexant sterically inhibits inward motions of TM domains by lodging deep in the orthosteric site and contacting all TM α-helices except TM1 (Fig. 2b, c). The shape of suvorexant in the ligand-binding pocket resembles a horseshoe, due to a boat conformation of the diazepane ring and intramolecular π-stacking between the aromatic benzoxazole and *p*-toluamide groups (Fig. 2b, c and Extended Data Fig. 3). A similar conformation of a suvorexant analogue was previously found in small-molecule crystals and by NMR experiments in solution[24], indicating that the horseshoe probably represents a low-free-energy state of the isolated ligand. Most of the ligand contacts involve van der Waals interactions or aromatic packing, with few direct polar interactions aside from a notable hydrogen bond from N324$^{6.55}$ to suvorexant's tertiary amide carbonyl. Several water-mediated hydrogen bonds form bridges between suvorexant and polar amino acids such as N324$^{6.55}$ and H350$^{7.39}$ (Fig. 2b, c). Although the effects of mutagenesis on suvorexant affinity to hOX$_2$R have not been reported, certain Ala mutants appear to have a broad deleterious effect on DORA binding[18]: W214$^{5.29}$ and Y223$^{5.38}$ do not directly participate in suvorexant binding, but are critical to the structural integrity of the ECL2 β-hairpin; F227$^{5.42}$ at the base of the

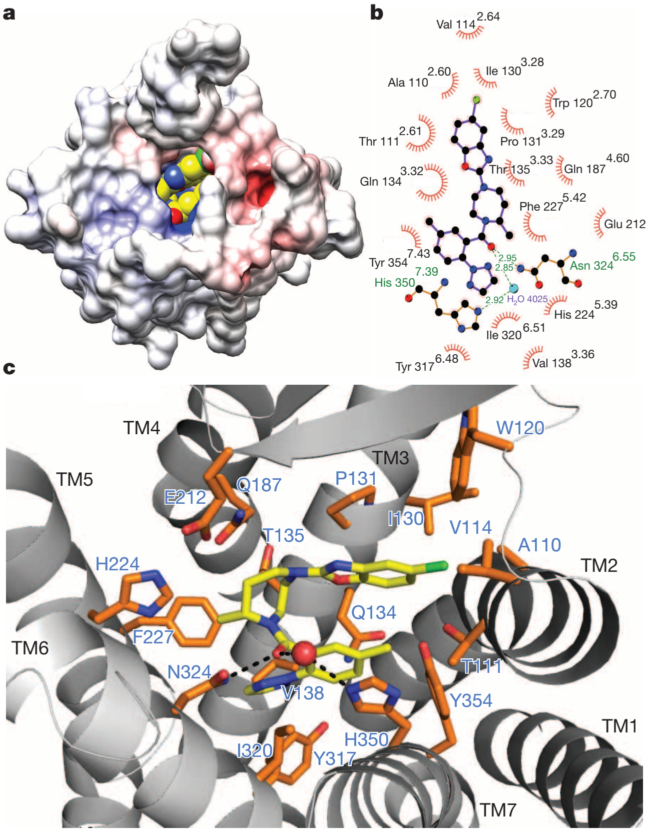

Figure 2 | Suvorexant interaction with hOX$_2$R. **a**, Solvent-accessible channel to the ligand-binding site. The solvent-accessible surface of the receptor is coloured according to electrostatic potential. Suvorexant is shown as spheres with yellow carbons. **b**, Two-dimensional schematic of contacts between suvorexant and the receptor. **c**, Three-dimensional interaction between suvorexant and hOX$_2$R, showing all residues within 4 Å of the ligand as sticks with orange carbons. Hydrogen bonds are shown as black dashes. H$_2$O 4025 is shown as a red sphere.

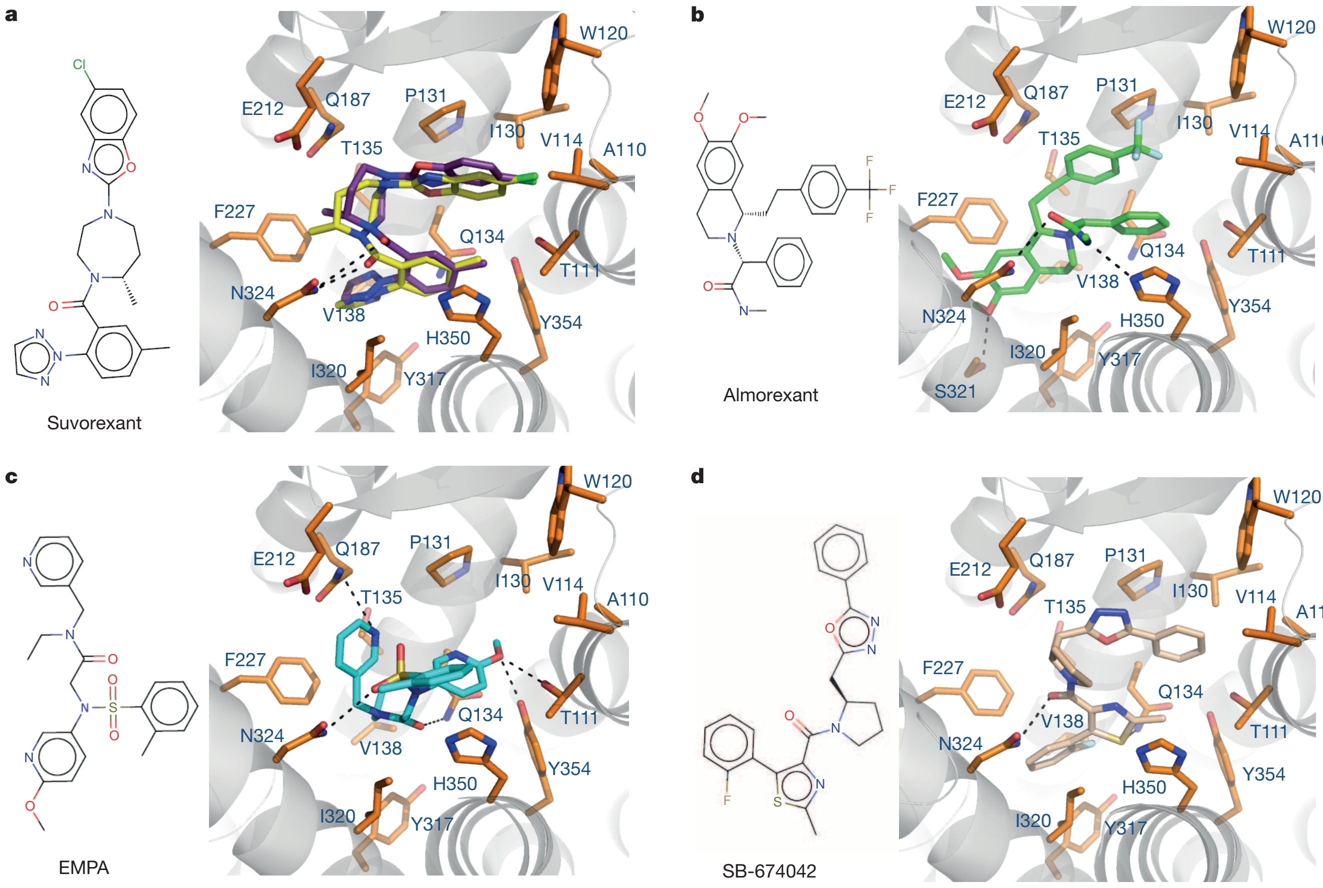

Figure 3 | Docked poses for synthetic orexin receptor antagonists. **a**, Left, chemical structure of suvorexant. Right, recapitulated binding mode of suvorexant (purple carbons) superimposed with the observed pose in the crystal structure (yellow carbons). Hydrogen bonds are shown as black dashes. **b**–**d**, Chemical structure and predicted binding mode of almorexant (green carbons) (**b**), EMPA (cyan carbons) (**c**) and SB-674042 (tan carbons) (**d**).

binding pocket packs against the methyl-diazepane ring; Y317$^{6.48}$ contacts the 1,2,3-triazole; and H350$^{7.39}$ π-stacks with the *p*-toluamide group. The residues surrounding suvorexant and the ligand entry channel are almost identical between hOX$_1$R and hOX$_2$R (Extended Data Figs 4 and 5), explaining suvorexant's ability to bind tightly and inhibit both receptors[9]. Out of 30 residues that are within 6 Å distance of suvorexant in the hOX$_2$R structure, only two amino acids are different compared with hOX$_1$R: T111$^{2.61}$ is changed to Ser and T135$^{3.33}$ is changed to Ala (overall sequence identity, 67%). This sequence conservation also implies that the 12-fold higher orexin-B affinity (and 40-fold higher potency) for hOX$_2$R over hOX$_1$R[25] is probably due to differences in interactions that are remote from the deeply membrane-embedded orthosteric binding pocket.

We have previously used computational docking methods to effectively predict interactions between a GPCR of known structure and small-molecule ligands[26]. With the newly available hOX$_2$R structure, we carried out molecular docking calculations (see Methods) to generate possible binding modes for three additional high-affinity orexin receptor antagonists that have chemical scaffolds distinct from suvorexant: almorexant[27], EMPA[28], and SB-674042 (ref. 29). As a control, we showed that our docking protocols were capable of accurately reproducing the interaction between suvorexant and hOX$_2$R in the crystal structure (Fig. 3a). Predicted poses for each of the other docked ligands establish a hydrogen bond with N324$^{6.55}$ (Fig. 3b–d), and two of the three adopt a π-stacked horseshoe-like conformation that mimics the binding of suvorexant (Fig. 3b, d). The amide functionality of almorexant forms a bidentate hydrogen bond with N324$^{6.55}$ and H350$^{7.39}$ (Fig. 3b), and mutation of the latter residue to Ala was shown experimentally to reduce binding affinity for hOX$_2$R[18]. In the predicted pose for EMPA, hydrogen bonds are established between the methoxy substituent on the 2-methoxypyridine and T111$^{2.61}$ and Y354$^{7.43}$ on the receptor (Fig. 3c), both of which are implicated in EMPA's interaction by mutational data[18,30]. In contrast to the other two molecules, no EMPA pose featured intramolecular π-stacking similar to suvorexant. For almorexant and EMPA, docking also yielded favourably scored second binding modes consistent with mutational data (Extended Data Fig. 6a, b). Finally, the predicted pose for SB-674042 closely resembles the binding mode of suvorexant, with its phenyl-oxadiazole overlapping almost perfectly with suvorexant's benzoxazole and its 2-methyl-thiazole overlapping with suvorexant's triazole (Fig. 3d). Overall, the prediction of intramolecular π-stacked conformations for multiple docked orexin receptor antagonists suggests that this property may be a general favourable design feature for synthetic molecules targeting the orthosteric site of hOX$_2$R.

We solved a high-resolution crystal structure of hOX$_2$R bound to the therapeutic compound suvorexant, providing a molecular framework for understanding DORA binding and stabilization of the inactive state by a salt-bridge network at the extracellular surface. Docking calculations predict putative stable binding modes for other orexin receptor antagonists, which are consistent with known mutational data. This knowledge will serve as a powerful tool in the design of improved agents that can activate or inactivate orexin signalling.

Online Content Methods, along with any additional Extended Data display items and Source Data, are available in the online version of the paper; references unique to these sections appear only in the online paper.

Received 16 September; accepted 4 November 2014.

1. Li, J., Hu, Z. & de Lecea, L. The hypocretins/orexins: integrators of multiple physiological functions. *Br. J. Pharmacol.* **171,** 332–350 (2014).

2. Michelson, D. *et al.* Safety and efficacy of suvorexant during 1-year treatment of insomnia with subsequent abrupt treatment discontinuation: a phase 3 randomised, double-blind, placebo-controlled trial. *Lancet Neurol.* **13,** 461–471 (2014).
3. Fredriksson, R., Lagerström, M. C., Lundin, L.-G. & Schiöth, H. B. The G-protein-coupled receptors in the human genome form five main families. Phylogenetic analysis, paralogon groups, and fingerprints. *Mol. Pharmacol.* **63,** 1256–1272 (2003).
4. Winrow, C. J. & Renger, J. J. Discovery and development of orexin receptor antagonists as therapeutics for insomnia. *Br. J. Pharmacol.* **171,** 283–293 (2014).
5. Zhu, Y. *et al.* Orexin receptor type-1 couples exclusively to pertussis toxin-insensitive G-proteins, while orexin receptor type-2 couples to both pertussis toxin-sensitive and -insensitive G-proteins. *J. Pharmacol. Sci.* **92,** 259–266 (2003).
6. Lin, L. *et al.* The sleep disorder canine narcolepsy is caused by a mutation in the hypocretin (orexin) receptor 2 gene. *Cell* **98,** 365–376 (1999).
7. Chemelli, R. M. *et al.* Narcolepsy in orexin knockout mice: molecular genetics of sleep regulation. *Cell* **98,** 437–451 (1999).
8. Nishino, S., Ripley, B., Overeem, S., Lammers, G. J. & Mignot, E. Hypocretin (orexin) deficiency in human narcolepsy. *Lancet* **355,** 39–40 (2000).
9. Cox, C. D. *et al.* Discovery of the dual orexin receptor antagonist [(7*R*)-4-(5-chloro-1,3-benzoxazol-2-yl)-7-methyl-1,4-diazepan-1-yl][5-methyl-2-(2*H*-1,2,3-triazol-2-yl)phenyl]methanone (MK-4305) for the treatment of insomnia. *J. Med. Chem.* **53,** 5320–5332 (2010).
10. Rosenbaum, D. M. *et al.* GPCR engineering yields high-resolution structural insights into 2-adrenergic receptor function. *Science* **318,** 1266–1273 (2007).
11. Warne, T. *et al.* Structure of a $\beta1$-adrenergic G-protein-coupled receptor. *Nature* **454,** 486–491 (2008).
12. Caffrey, M. Crystallizing membrane proteins for structure determination: use of lipidic mesophases. *Annu. Rev. Biophys.* **38,** 29–51 (2009).
13. White, J. F. *et al.* Structure of the agonist-bound neurotensin receptor. *Nature* **490,** 508–513 (2012).
14. Egloff, P. *et al.* Structure of signaling-competent neurotensin receptor 1 obtained by directed evolution in *Escherichia coli*. *Proc. Natl Acad. Sci. USA* **111,** E655–E662 (2014).
15. Horcajada, C., Guinovart, J. J., Fita, I. & Ferrer, J. C. Crystal structure of an archaeal glycogen synthase: insights into oligomerization and substrate binding of eukaryotic glycogen synthases. *J. Biol. Chem.* **281,** 2923–2931 (2006).
16. Manglik, A. *et al.* Crystal structure of the μ-opioid receptor bound to a morphinan antagonist. *Nature* **485,** 321–326 (2012).
17. Wu, B. *et al.* Structures of the CXCR4 chemokine GPCR with small-molecule and cyclic peptide antagonists. *Science* **330,** 1066–1071 (2010).
18. Malherbe, P. *et al.* Mapping the binding pocket of dual antagonist almorexant to human orexin 1 and orexin 2 receptors: comparison with the selective OX_1 antagonist SB-674042 and the selective OX_2 antagonist *N*-ethyl-2-[(6-methoxy-pyridin-3-yl)-(toluene-2-sulfonyl)-amino]-*N*-pyridin-3-ylmethyl-acetamide (EMPA). *Mol. Pharmacol.* **78,** 81–93 (2010).
19. Kruse, A. C. *et al.* Structure and dynamics of the M3 muscarinic acetylcholine receptor. *Nature* **482,** 552–556 (2012).
20. Ballesteros, J. A. Activation of the β_2-adrenergic receptor involves disruption of an ionic lock between the cytoplasmic ends of transmembrane segments 3 and 6. *J. Biol. Chem.* **276,** 29171–29177 (2001).
21. Bokoch, M. P. *et al.* Ligand-specific regulation of the extracellular surface of a G-protein-coupled receptor. *Nature* **463,** 108–112 (2010).
22. Rasmussen, S. G. F. *et al.* Structure of a nanobody-stabilized active state of the β_2 adrenoceptor. *Nature* **469,** 175–180 (2011).
23. Kruse, A. C. *et al.* Activation and allosteric modulation of a muscarinic acetylcholine receptor. *Nature* **504,** 101–106 (2013).
24. Cox, C. D. *et al.* Conformational analysis of *N*,*N*-disubstituted-1,4-diazepane orexin receptor antagonists and implications for receptor binding. *Bioorg. Med. Chem. Lett.* **19,** 2997–3001 (2009).
25. Sakurai, T. *et al.* Orexins and orexin receptors: a family of hypothalamic neuropeptides and G protein-coupled receptors that regulate feeding behavior. *Cell* **92,** 573–585 (1998).
26. Kolb, P. *et al.* Structure-based discovery of β_2-adrenergic receptor ligands. *Proc. Natl Acad. Sci. USA* **106,** 6843–6848 (2009).
27. Brisbare-Roch, C. *et al.* Promotion of sleep by targeting the orexin system in rats, dogs and humans. *Nature Med.* **13,** 150–155 (2007).
28. Malherbe, P. *et al.* Biochemical and behavioural characterization of EMPA, a novel high-affinity, selective antagonist for the OX_2 receptor. *Br. J. Pharmacol.* **156,** 1326–1341 (2009).
29. Langmead, C. J. *et al.* Characterisation of the binding of [^{3}H]-SB-674042, a novel nonpeptide antagonist, to the human orexin-1 receptor. *Br. J. Pharmacol.* **141,** 340–346 (2004).
30. Tran, D.-T. *et al.* Chimeric, mutant orexin receptors show key interactions between orexin receptors, peptides and antagonists. *Eur. J. Pharmacol.* **667,** 120–128 (2011).

Supplementary Information is available in the online version of the paper.

Acknowledgements We acknowledge support from the Welch Foundation (I-1770 to D.M.R.), the Searle Scholars Program (D.M.R.), a Packard Foundation Fellowship (D.M.R.), an Emmy Noether Fellowship of the German Research Foundation (KO-4095/1-1 to P.K.) and COST Action GLISTEN (CM1207 to P.K.). We thank D. Borek and Z. Otwinowski for assistance with diffraction data processing. The National Institute of General Medical Sciences and National Cancer Institute Structural Biology Facility at the Advanced Photon Source is funded in whole or in part with federal funds from the National Cancer Institute (ACB-12002) and the National Institute of General Medical Sciences (AGM-12006).

Author Contributions J.Y. expressed, purified and crystallized the hOX$_2$R–PGS fusion protein, collected diffraction data, and solved the structure. J.C.M. performed computational docking experiments on synthetic orexin receptor antagonists. P.K. supervised and performed computational docking experiments. D.M.R. supervised the overall project, assisted with collection of diffraction data and wrote the manuscript. All authors discussed the results and commented on the manuscript.

Author Information Atomic coordinates and structure factors for the reported crystal structure have been deposited in the PDB under accession 4RNB. Reprints and permissions information is available at www.nature.com/reprints. The authors declare no competing financial interests. Readers are welcome to comment on the online version of the paper. Correspondence and requests for materials should be addressed to D.M.R. (dan.rosenbaum@utsouthwestern.edu).

METHODS

Cloning, expression and purification. A DNA fragment corresponding to residues 1–386 of hOX_2R was cloned into a modified pFastBac (Invitrogen) baculovirus expression vector with the haemagglutinin (HA) signal sequence followed by the Flag tag at the N terminus[31]. The 58 C-terminal (intracellular) amino acids of hOX_2R were omitted owing to the prediction that they are unstructured and do not comprise part of the 7TM bundle. The hOX_2R–PGS fusion protein construct was generated by substituting a synthetic DNA fragment containing the 196-amino-acid coding sequence of *P. abysii* glycogen synthase (PDB accession 2BFW)[15] for residues 255–293 in the hOX_2R ICL3 using an adapted Multi-Site Quickchange protocol (Stratagene). For purification, a deca-histidine tag was added at the C terminus. The resulting construct was transfected into Sf9 cells to produce a recombinant baculovirus with the Bac-to-Bac system (Invitrogen). Sf9 cultures were infected with recombinant baculovirus at a cell density of 3×10^6 per ml and 1 μM suvorexant was added to the media. Infected cells were grown for 48 h at 27 °C, and cells were harvested and stored at −80 °C for future use.

Sf9 cell membranes were lysed in a hypotonic buffer containing 10 mM Tris pH 7.5, 1 mM EDTA, 160 $\mu g\,ml^{-1}$ benzamidine, 100 $\mu g\,ml^{-1}$ leupeptin, 2 $mg\,ml^{-1}$ iodoacetamide and 1 μM suvorexant (Selleck Chemicals). Lysed membranes were re-suspended and homogenized by dounce in a buffer containing 50 mM Tris pH 7.5, 500 mM NaCl, 1% (w/v) *n*-dodecyl-β-D-maltopyranoside (DDM; Anatrace), 0.2% sodium cholate, 0.2% cholesteryl hemi-succinate (CHS), 10% glycerol, 2 $mg\,ml^{-1}$ iodoacetamide and 5 μM suvorexant. Solubilization proceeded for 1 h at 4 °C, followed by ultracentrifugation for 30 min at 100,000*g*. After centrifugation, the solubilized supernatant supplemented with 20 mM imidazole was incubated with Ni-NTA agarose beads (GE Healthcare) in batch-binding mode for 3 h at 4 °C. After binding, beads were washed with 15 column volumes of Ni-NTA buffer: 50 mM Tris pH 7.5, 500 mM NaCl, 0.1% DDM, 0.02% sodium cholate, 0.02% CHS, 5% glycerol, 50 mM imidazole and 5 μM suvorexant. Protein was eluted with 5 column volumes of Ni-NTA wash buffer with 200 mM imidazole. The eluate from nickel-affinity chromatography was supplemented with 2 mM calcium and loaded onto M1 anti-Flag affinity beads (Sigma). Detergent was exchanged on the M1 resin from DDM to 0.05% lauryl maltose neopentyl glycol (LMNG; Anatrace). Receptor was eluted from the M1 beads with 200 $\mu g\,ml^{-1}$ Flag peptide plus 5 mM EDTA. To remove N-linked glycan from the receptor, PNGaseF (NEB) was added and the reaction was incubated at 4 °C overnight. Finally, protein was concentrated in a 100 kDa cut-off Vivaspin column (Sartorius) and run on a Superdex 200 size exclusion column (GE Healthcare). The purified protein displayed a single monodisperse peak in the size exclusion profile (Extended Data Fig. 1a), and was >95% pure as judged by SDS–PAGE gel electrophoresis (Extended Data Fig. 1b).

Crystallization. Purified receptor was concentrated to $>30\ mg\,ml^{-1}$ using a Vivaspin concentrator with a 100 kDa molecular weight cut-off (Sartorius) and subjected to crystallization by the *in meso* method[32]. The concentrated protein was reconstituted into a lipid mixture containing monoolein plus 10% (w/w) cholesterol (Sigma), where the protein solution:lipid mass ratio was 2:3. Receptor and lipid components were mixed at room temperature using a syringe mixing apparatus. Crystallization experiments were carried out in 96-well glass sandwich plates (Molecular Dimensions) by a Gryphon LCP crystallization robot (Art Robbins Instruments) using a 40 nl protein cubic phase overlaid with 800 nl precipitant solution. Crystallization plates were incubated at 20 °C and initial crystals appeared after 24 h in a precipitant condition consisting of 100 mM MES pH 6.0, 30% PEG 400, 200 mM sodium formate. Crystals matured to full size in 3 days. Improved crystals were obtained in a condition consisting of 100 mM sodium citrate pH 5.9, 31% PEG 400, 200 mM sodium formate, 3% 2,5-hexanediol (Extended Data Fig. 2). Crystals were cryo-protected by harvesting directly from the LCP/precipitant setups with 100 μm MiTeGen loops and flash freezing in liquid nitrogen.

Data collection and processing. All diffraction data were collected at the 23ID-D beamline (GM/CA-CAT) at the Advanced Photon Source, Argonne National Laboratory, which is equipped with a Pilatus3 6M detector. Data sets were acquired using a 20 μm collimated minibeam with 1.033 Å wavelength X-rays. For a typical crystal, twenty-five 0.4° oscillation images were collected, with 1 s exposure and without attenuation of the beam, before radiation damage became excessive. Diffraction data from 52 crystals were merged into one complete data set. The resolution limit was set at 2.5 Å after anisotropy analysis with HKL3000 (ref. 33) (Extended Data Table 1).

Structure determination and refinement. The structure of hOX_2R–PGS was solved by molecular replacement with Phaser[34] in Phenix[35]. The PGS domain (PDB accession 2BFW)[15] and μ-OR (PDB accession 4DKL)[16] were used as independent search models after analysis with Sculptor in Phenix[35]. The resulting solution was improved by auto-building in Buccaneer[36] and by manual iterative building in Coot[37] followed by refinement with Phenix. Translation–libration–screw (TLS) refinement was employed to model atomic displacement factors, with TLS groups generated by the TLSMD web server[38]. Initial coordinates and refinement parameters for the suvorexant ligand were prepared with the PRODRG[39] web server. An elongated feature in the electron density map, which was observed within the bilayer region, was modelled as oleic acid. MolProbity[40] was used to evaluate the final structure. In the Ramachandran plot, 98.1% of residues were in favoured regions and 1.9% of residues were in allowed regions. The statistics for data collection and refinement are included in Extended Data Table 1. Figures were prepared using PyMol (Schrodinger LLC). The electrostatic potential surface shown in Fig. 2a was calculated using DelPhi[41], and the ligand contact map shown in Fig. 2b was made using LIGPLOT[42].

Small-molecule docking. Docking calculations were done with DOCK 3.6 (refs 43, 44) and AutoDock[45] in order to obtain more diverse solutions. Dockings of the three orexin receptor antagonists to hOX_2R with AutoDock v.4.2 (ref. 45) used a static receptor and a flexible ligand. Receptor and ligand preparation was performed with Autodock Tools (ADT). The reference grid box ($60 \times 60 \times 60$ points and 0.375 Å of grid spacing) surrounded the suvorexant pose in the hOX_2R structure, allowing free ligand rotation and displacement. A genetic algorithm was used for exhaustive conformational sampling, and run 100 times with different random seeds.

Docking of all compounds was also performed with DOCK 3.6 (refs 43, 44). Anchor spheres to guide the placement of the molecules were distributed based on the molecular surface of the receptor and the pose of suvorexant in the hOX_2R structure. The receptor was fixed during calculations and prepared for docking such that ionizable side chains were charged, except for histidines, for which protonation was modelled based on protein environment.

To further enrich conformational space, small-molecule conformations were generated with OMEGA[46] (OpenEye), using default settings except for the forcefield (mmff94s); an increased maximum number of conformations (300); an enlarged energy window (20); and a decreased r.m.s.d. cut-off (0.3). Representative conformations were then manually positioned in the binding pocket and minimized using the CHARMm22 forcefield (Accelrys), not constraining $N324^{6.55}$ and $H350^{7.39}$ to allow for side-chain flips. Expert criteria, namely satisfaction of hydrogen bonds, matching of polar and apolar groups, and consistency with mutational data, were used in the inspection and final selection of the poses. Finally, all poses, including the DOCK- and AutoDock-derived ones were evaluated with the DSX scoring function[47]. The poses shown were among the ones with the most favourable interaction scores. Two-dimensional chemical structures were drawn with Marvin 6.2.0 (Chemaxon).

31. Kobilka, B. K. Amino and carboxyl terminal modifications to facilitate the production and purification of a G protein-coupled receptor. *Anal. Biochem.* **231,** 269–271 (1995).
32. Caffrey, M. & Cherezov, V. Crystallizing membrane proteins using lipidic mesophases. *Nature Protocols* **4,** 706–731 (2009).
33. Otwinowski, Z. & Minor, W. Processing of X-ray diffraction data collected in oscillation mode. *Methods Enzymol.* **276,** 307–326 (1997).
34. McCoy, A. J. *et al.* Phaser crystallographic software. *J. Appl. Crystallogr.* **40,** 658–674 (2007).
35. Adams, P. D. *et al.* PHENIX: a comprehensive Python-based system for macromolecular structure solution. *Acta Crystallogr. D* **66,** 213–221 (2010).
36. Cowtan, K. Fitting molecular fragments into electron density. *Acta Crystallogr. D* **64,** 83–89 (2008).
37. Emsley, P., Lohkamp, B., Scott, W. G. & Cowtan, K. Features and development of Coot. *Acta Crystallogr. D* **66,** 486–501 (2010).
38. Painter, J. & Merritt, E. A. TLSMD web server for the generation of multi-group TLS models. *J. Appl. Crystallogr.* **29,** 109--111 (2006).
39. Schüttelkopf, A. W. & van Aalten, D. M. F. PRODRG: a tool for high-throughput crystallography of protein-ligand complexes. *Acta Crystallogr. D* **60,** 1355–1363 (2004).
40. Chen, V. B. *et al.* MolProbity: all-atom structure validation for macromolecular crystallography. *Acta Crystallogr. D* **66,** 12–21 (2010).
41. Rocchia, W., Alexov, E. & Honig, B. Extending the applicability of the nonlinear Poisson–Boltzmann equation: multiple dielectric constants and multivalent ions. *J. Phys. Chem. B* **105,** 6507–6514 (2001).
42. Wallace, A. C., Laskowski, R. A. & Thornton, J. M. LIGPLOT: a program to generate schematic diagrams of protein-ligand interactions. *Protein Eng.* **8,** 127–134 (1995).
43. Irwin, J. J. *et al.* Automated docking screens: a feasibility study. *J. Med. Chem.* **52,** 5712–5720 (2009).
44. Mysinger, M. M. & Shoichet, B. K. Rapid context-dependent ligand desolvation in molecular docking. *J. Chem. Inf. Model.* **50,** 1561–1573 (2010).
45. Morris, G. M. *et al.* AutoDock4 and AutoDockTools4: automated docking with selective receptor flexibility. *J. Comput. Chem.* **30,** 2785–2791 (2009).
46. Kirchmair, J., Wolber, G., Laggner, C. & Langer, T. Comparative performance assessment of the conformational model generators Omega and Catalyst: a large-scale survey on the retrieval of protein-bound ligand conformations. *J. Chem. Inf. Model.* **46,** 1848–1861 (2006).
47. Neudert, G. & Klebe, G. *DSX*: a knowledge-based scoring function for the assessment of protein-ligand complexes. *J. Chem. Inf. Model.* **51,** 2731–2745 (2011).

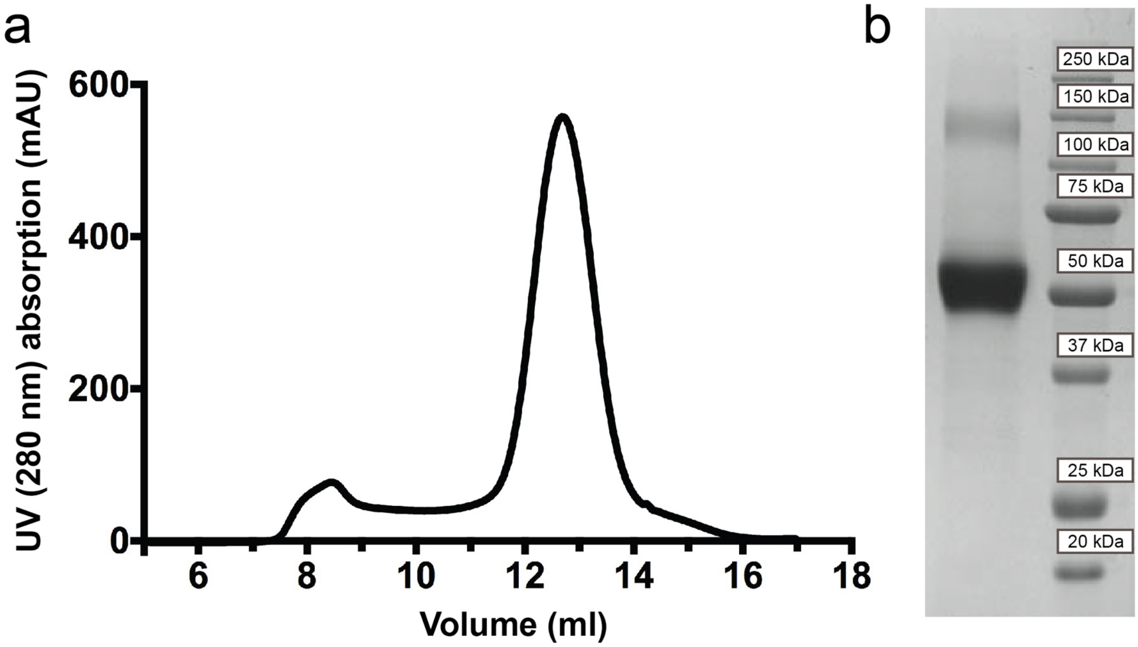

Extended Data Figure 1 | Purification of crystallization-grade hOX$_2$R–PGS. **a**, Superdex 200 gel filtration profile of hOX$_2$R–PGS purified by nickel immobilized-metal affinity chromatography (Ni-IMAC) and M1-Flag immunoaffinity chromatography. **b**, Coommassie-stained polyacrylamide gel electrophoresis (PAGE) of the isolated peak fraction from gel filtration.

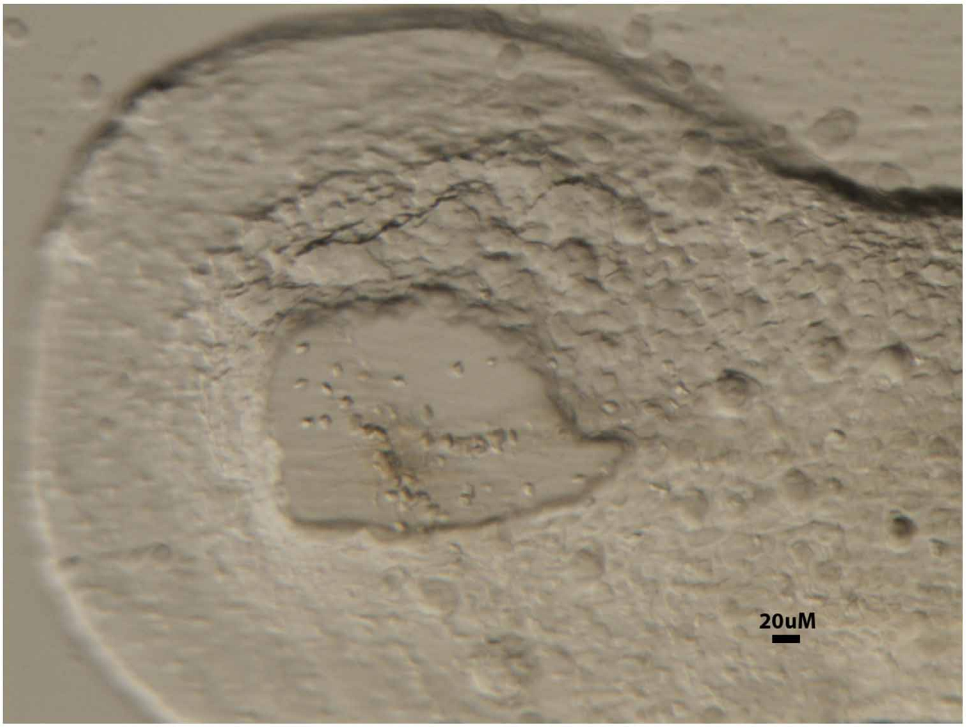

Extended Data Figure 2 | Lipidic cubic phase crystallization setup for hOX$_2$R–PGS. The image shows representative microcrystals of the hOX$_2$R–PGS protein that were harvested to produce high-resolution diffraction.

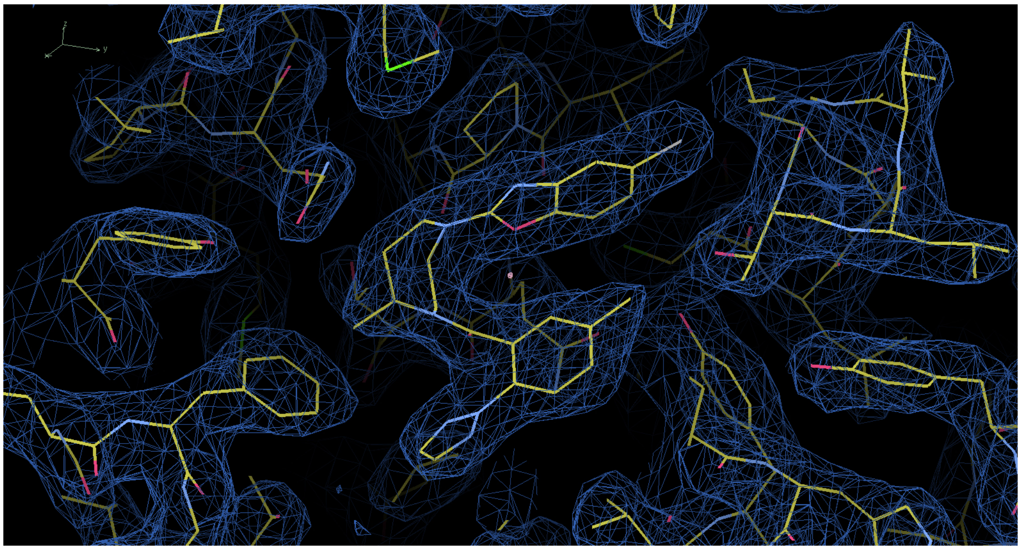

Extended Data Figure 3 | Electron density map for suvorexant and surrounding residues. The $2F_o - F_c$ electron density map is contoured at 1.2σ.

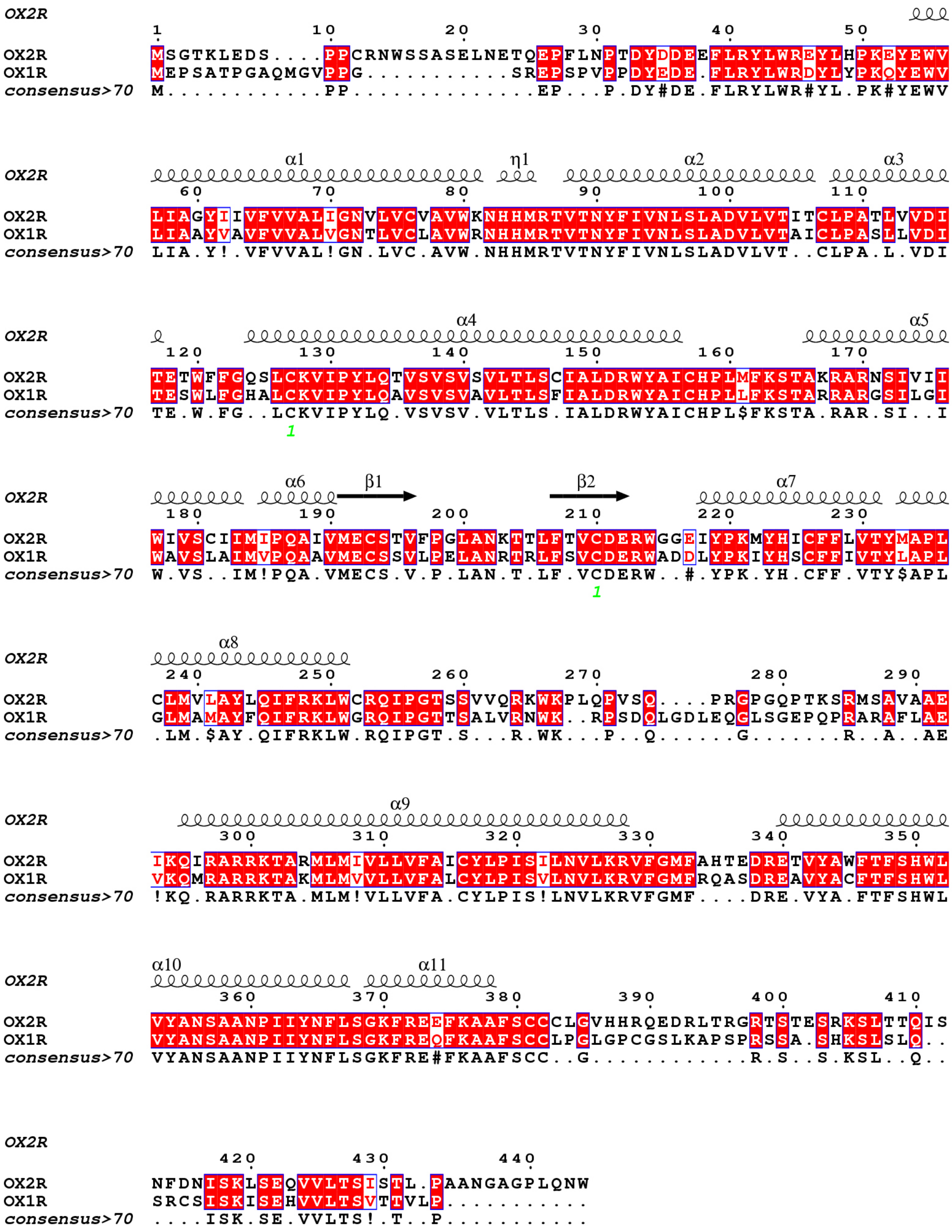

```
OX2R
               1         10        20        30        40        50
OX2R           MSGTKLEDS....PPCRNWSSASELNETQEPFLNPTDYDDEEFLRYLWREYLHPKEYEWV
OX1R           MEPSATPGAQMGVPPG...........SREPSPVPPDYEDE.FLRYLWRDYLYPKQYEWV
consensus>70   M............PP..............EP...P.DY#DE.FLRYLWR#YL.PK#YEWV

                          α1          η1       α2              α3
OX2R
                  60        70        80        90        100       110
OX2R           LIAGYIIVFVVALIGNVLVCVAVWKNHHMRTVTNYFIVNLSLADVLVTITCLPATLVVDI
OX1R           LIAAYVAVFVVALVGNTLVCLAVWRNHHMRTVTNYFIVNLSLADVLVTAICLPASLLVDI
consensus>70   LIA.Y!.VFVVAL!GN.LVC.AVW.NHHMRTVTNYFIVNLSLADVLVT..CLPA.L.VDI

                                         α4                       α5
OX2R
                120       130       140       150       160       170
OX2R           TETWFFGQSLCKVIPYLQTVSVSVSVLTLSCIALDRWYAICHPLMFKSTAKRARNSIVII
OX1R           TESWLFGHALCKVIPYLQAVSVSVAVLTLSFIALDRWYAICHPLLFKSTARRARGSILGI
consensus>70   TE.W.FG..LCKVIPYLQ.VSVSV.VLTLS.IALDRWYAICHPL$FKSTA.RAR.SI..I
                         1

                         α6  β1              β2              α7
OX2R
                180       190       200       210       220       230
OX2R           WIVSCIIMIPQAIVMECSTVFPGLANKTTLFTVCDERWGGEIYPKMYHICFFLVTYMAPL
OX1R           WAVSLAIMVPQAAVMECSSVLPELANRTRLFSVCDERWADDLYPKIYHSCFFIVTYLAPL
consensus>70   W.VS..IM!PQA.VMECS.V.P.LAN.T.LF.VCDERW..#.YPK.YH.CFF.VTY$APL
                                                1

                     α8
OX2R
                240       250       260       270           280       290
OX2R           CLMVLAYLQIFRKLWCRQIPGTSSVVQRKWKPLQPVSQ....PRGPGQPTKSRMSAVAAE
OX1R           GLMAMAYFQIFRKLWGRQIPGTTSALVRNWK..RPSDQLGDLEQGLSGEPQPRARAFLAE
consensus>70   .LM.$AY.QIFRKLW.RQIPGT.S...R.WK...P..Q......G.......R..A..AE

                                       α9
OX2R
                    300       310       320       330       340       350
OX2R           IKQIRARRKTARMLMIVLLVFAICYLPISILNVLKRVFGMFAHTEDRETVYAWFTFSHWL
OX1R           VKQMRARRKTAKMLMVVLLVFALCYLPISVLNVLKRVFGMFRQASDREAVYACFTFSHWL
consensus>70   !KQ.RARRKTA.MLM!VLLVFA.CYLPIS!LNVLKRVFGMF....DRE.VYA.FTFSHWL

               α10                 α11
OX2R
                    360       370       380       390       400       410
OX2R           VYANSAANPIIYNFLSGKFREEFKAAFSCCCLGVHHRQEDRLTRGRTSTESRKSLTTQIS
OX1R           VYANSAANPIIYNFLSGKFREQFKAAFSCCLPGLGPCGSLKAPSPRSSA.SHKSLSLQ..
consensus>70   VYANSAANPIIYNFLSGKFRE#FKAAFSCC..G............R.S..S.KSL..Q..

OX2R
                    420       430       440
OX2R           NFDNISKLSEQVVLTSISTL.PAANGAGPLQNW
OX1R           SRCSISKISEHVVLTSVTTVLP...........
consensus>70   ....ISK.SE.VVLTS!.T..P...........
```

Extended Data Figure 4 | Sequence alignment between hOX_2R and hOX_1R. Positions that are identical between the two receptors are highlighted with a red background.

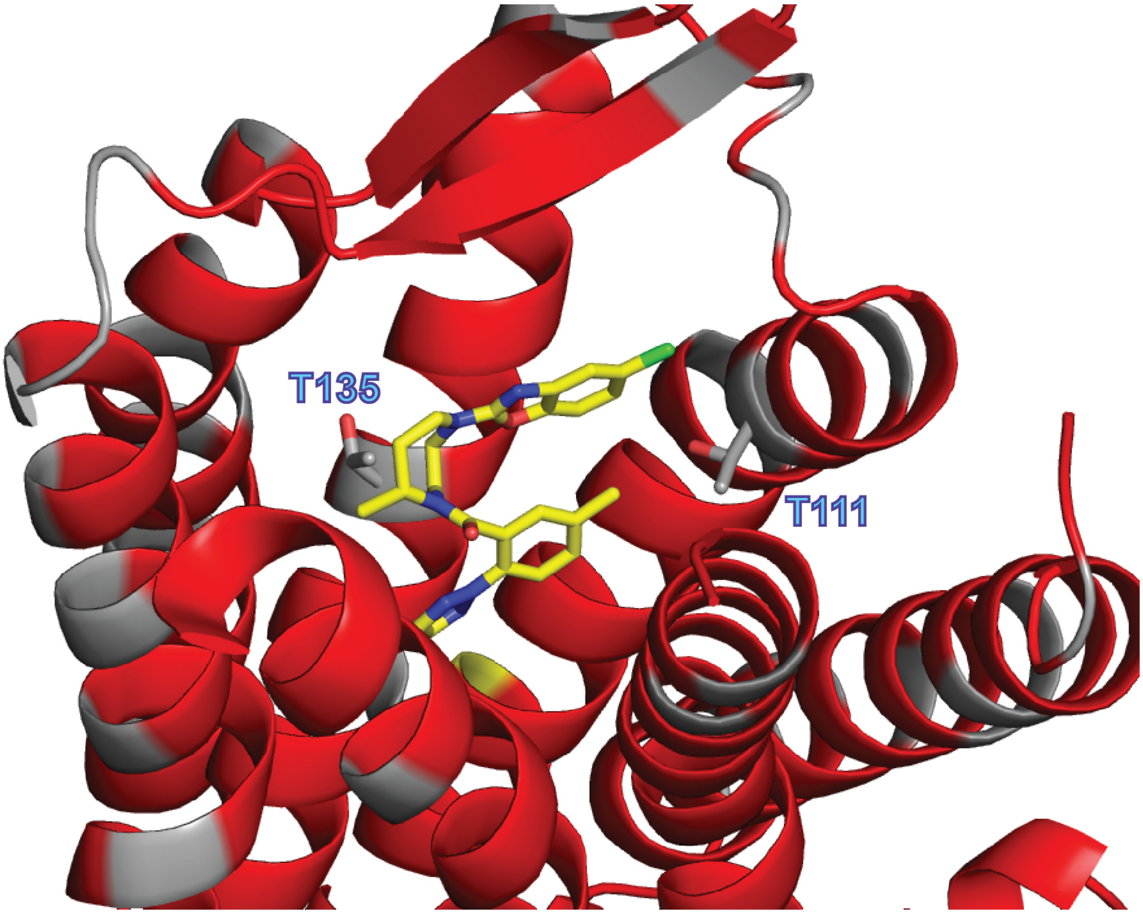

Extended Data Figure 5 | Conservation of the orthosteric binding pocket between hOX$_2$R and hOX$_1$R. Structure of the extracellular region of hOX$_2$R, with residues that are identical between hOX$_2$R and hOX$_1$R coloured red, and residues that are different coloured grey. T111$^{2.61}$ (to Ser) and T135$^{3.33}$ (to Ala) are the only residues within 6 Å of suvorexant that are different between the two GPCRs. ECL3 is removed for clarity.

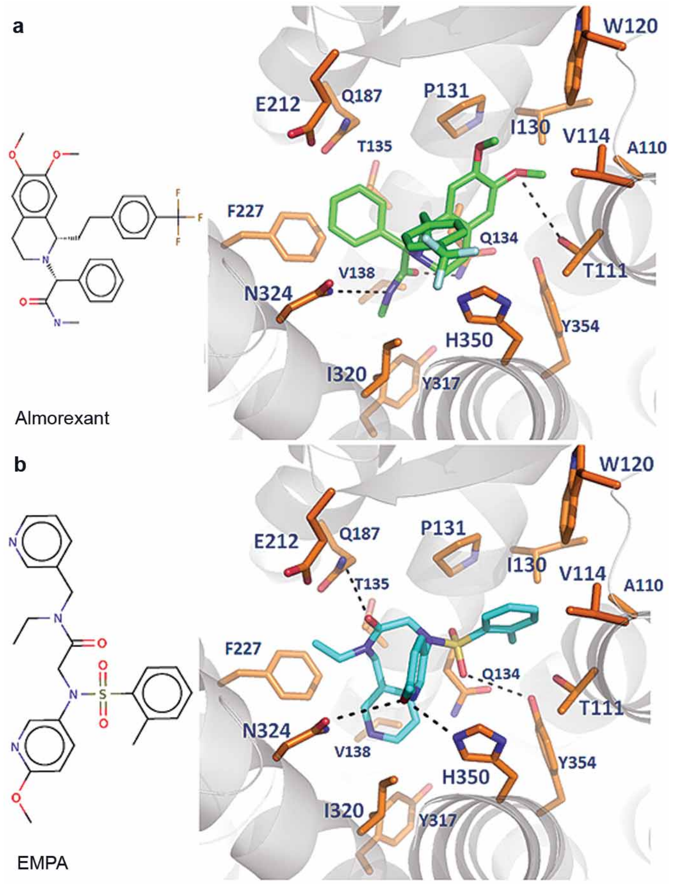

Extended Data Figure 6 | Alternative docked poses for almorexant and EMPA. **a**, Left, chemical structure of almorexant. Right, second docked pose of almorexant (green carbons) that was favourably scored and in agreement with mutational data. **b**, Left, chemical structure of EMPA. Right, second docked pose of EMPA (cyan carbons) that was favourably scored and in agreement with mutational data.

Extended Data Table 1 | Data collection and refinement statistics

	hOX$_2$R-PGS[*]
Data collection	
Space group	C2
Cell dimensions	
a, b, c (Å)	94.36, 75.82, 96.30
α, β, γ (°)	90.00, 111.71, 90.00
Resolution (Å)	50.00(2.50) [†]
R_{sym} or R_{merge} [‡]	0.21(N/A)
$I/\sigma I$ [§]	10.90/(0.86)
	a*, (0.26)
	b*, (2.00)
	c*, (3.80)
Completeness (%)	99.90(99.00)
Redundancy	14.30(5.9)
Refinement	
Resolution (Å)	43.70-2.50 (2.6-2.50)
No. reflections	18,772
$R_{work/}$ R_{free}	0.19/0.24 (0.26/0.31)
No. atoms	
Protein	3,810
Ligand/ion	32
Water	36
B-factors	
Receptor	42.40
Fusion protein	48.90
Ligand/ion	26.90
Other (Lipid and water)	39.35
R.m.s deviations	
Bond lengths (Å)	0.004
Bond angles (º)	0.77

[*] Diffraction data from 52 crystals were merged into a complete data set.

[†] Highest-resolution shell is shown in parenthesis.

[‡] R_{merge} higher than 1 is statistically meaningless, therefore Scalepack (HKL3000, ref. 33) does not report it.

[§] Crystals diffracted anisotropically. The correction for anisotropy was applied during scaling with Scalepack (HKL3000). $I/\sigma I$ values (a*, b* and c*) for the highest-resolution shell (2.62–2.5 Å) were calculated by dividing mean intensity values in each direction with average error values.